Lawrence Berkeley National Laboratory

Title

Thermo-hydrologic processes in maar eruptions: The role of vapor transport and condensation

Permalink

https://escholarship.org/uc/item/2sx7s2kg

Authors

Anderson, Emily S
Ort, Michael H
Oldenburg, Curtis M

Peer reviewed

1

2 Thermo-Hydrologic Processes in Maar Eruptions:

3 The Role of Vapor Transport and Condensation

4

5 Emily S. Anderson[1], Michael H. Ort[1], Curtis M. Oldenburg[2]

6

7 [1] School of Earth and Sustainability, Box 4099, Northern Arizona University,

8 Flagstaff, AZ 86011 USA

9

10 [2] Energy Geosciences Division, Lawrence Berkeley National Laboratory, 1 Cyclotron Rd.,

11 Berkeley, CA 94720 USA

12

13

18

Introduction

Phreatomagmatic eruptions occur when magma interacts directly with water or slurries, commonly from groundwater in the shallow crust, resulting in rapid conversion of thermal energy to mechanical energy in a set of processes known as molten fuel-coolant interaction (MFCI). The efficiency of MFCI is controlled by properties of the magma and coolant, contact surface geometry, and system conditions, such as pressure and temperature; phreatomagmatic behavior can range from passive thermal granulation to violent thermohydraulic explosions (Zimanowski et al., 2015). Maar-diatreme eruptions, characterized by repetitive phreatomagmatic explosions, can form in a wide range of near-surface environments, from soft-sediment substrate (e.g., Tecuitlapa, Mexico, Ort and Carrasco-Núñez, 2009; Hopi Buttes, AZ, Lefebvre et al., 2013) to hard, fractured country rock (e.g., West Eifel volcanic field, Germany and Massif Central, France, Lorenz, 2003). Country-rock structure, including faults and joints, rock type, and shallow crustal hydrologic properties, can influence an eruption's behavior by controlling how much and at what rate water can be supplied to the magma (hydraulic flow rate), and determining the sediment: water ratio in the case of soft-sediment substrate eruptions. In a "soft" substrate environment, volcanic tremor can lead to liquefaction of saturated sediment, producing a slurry that may then interact with magma in unique ways (White, 1996; Auer, et al., 2006).

Studies of maars around the world have shown the importance of magma-water interaction, but have not answered some fundamental questions about how aqueous-phase water was present and available to interact with magma throughout an eruptive episode. We have carried out field investigations and numerical modeling directed at answering the following questions:

42   1. In areas with very deep water tables, how is the necessary quantity of liquid water

43   supplied to the shallow subsurface to produce phreatomagmatic explosions?

44   2. How is liquid water continuously supplied to sustain a phreatomagmatic eruption

45   without being depleted through explosions and vaporization?

46   In this paper, we describe a potential mechanism, the heat-pipe process (e.g., Schubert

47 and Straus, 1979; Pruess, 1985), by which water in shallow crustal systems may be transported

48 upward as vapor to levels higher in the subsurface where it condenses. By this mechanism, heat

49 from shallow intrusions associated with the same eruption can potentially redistribute water to

50 produce water-saturated domains at levels above the regional water table depth, and these

51 domains, if rapidly intersected by magma, could lead to shallow (eruptible) phreatomagmatic

52 explosions, provided other conditions are met. We demonstrate the mechanism of upward vapor

53 transport and condensation by numerical simulations using TOUGH2 (Pruess et al, 2011) for an

54 idealized shallow crustal system heated by magma. Our work suggests that knowledge of the

55 hydraulic properties (e.g., permeability and fracture density) of bedrock is critical to

56 understanding how water (both vapor and aqueous phases) may move through and interact with

57 magma in the subsurface in the event of a magmatic intrusion.

58

59   *1.1. Background and Prior Work*

60   Maar-diatremes are formed by repeated magma-groundwater explosions. A maar is a

61 broad crater cutting below the pre-eruptive surface enclosed by a <30-m-high tephra ring of

62 repetitively bedded pyroclastic deposits (Fig. 1; Valentine and White, 2012; de Silva and

63 Lindsay, 2015). Diatremes are debris-filled conduits beneath maars that form as explosions

64 recycle wall rock and juvenile material. Early models of diatreme development attributed their

3

65 formation to progressively deepening MFCI explosions as groundwater depleted and a "cone of

66 depression" formed in the water table (Lorenz, 1986). In a current conceptual model (Fig. 1;

67 Valentine and White, 2012), explosions may occur at any depth where groundwater is below the

68 critical pressure of water (P_{crit} = 22.5 MPa). As explosions progressively disrupt the shallow

69 subsurface, broken-up material slumps into the diatreme/conduit, further widening the structure

70 and producing a roughly conical diatreme that may extend to depths of 2 – 2.5 km, although

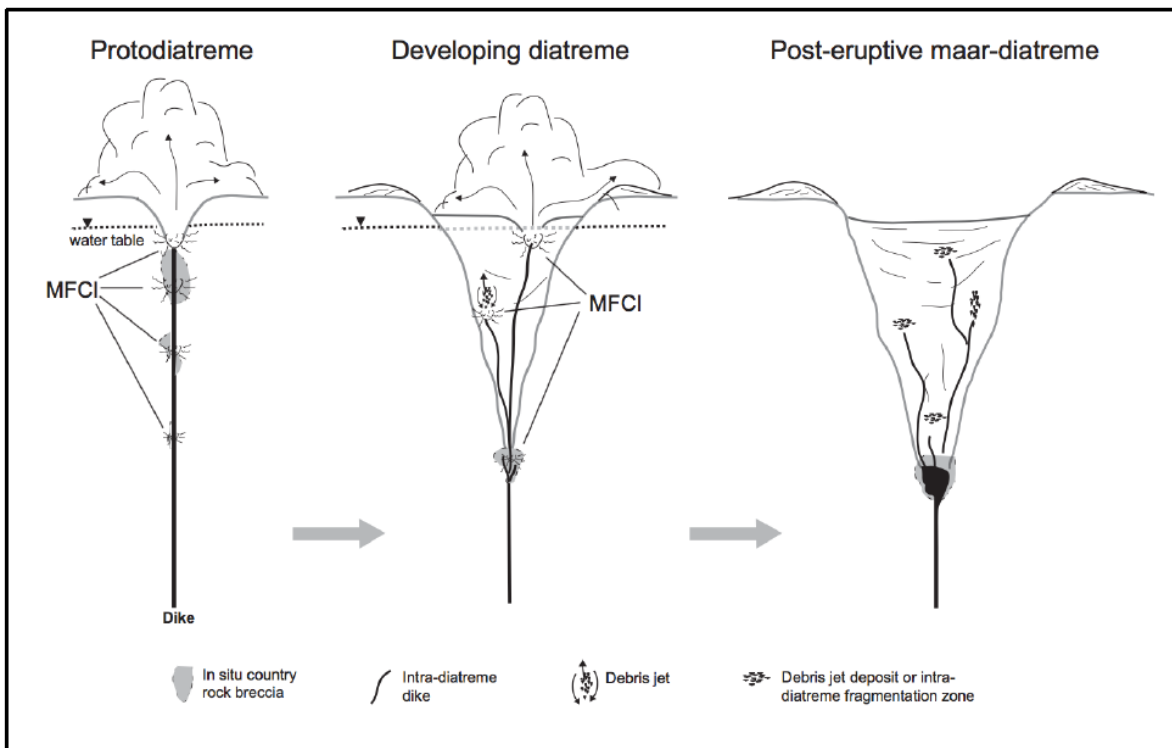71 shallower is more common (Valentine and White, 2012).

Figure 1: Modern conceptual model of maar-diatreme formation from Valentine and White (2012). Explosions may occur at any depth below the critical pressure of water, though shallow explosions are generally most efficient. The water table is probably maintained at a constant level throughout eruption, but debris jets and upward recycling within the diatreme may also assist in moving water through diatreme fill. MFCI = molten fuel-coolant interaction.

72

73   Valentine et al. (2014) estimated explosion energies in typical phreatomagmatic eruptions

74 based on theoretical, field, and limited experimental data, and combined this information with

well-documented phenomenology of subsurface explosions that defines conditions under which explosions are contained in the subsurface versus ejecting large quantities of material onto crater rims. They concluded that explosions do occur over a range of depths throughout an eruption, but generally, because the strength of explosions tends to lie within a certain range, only those occurring above ~200 m, and mostly above ~100 m, are able to throw material out of the crater to form the tephra ring and excavate the crater. Deeper explosions rarely vent to the surface, instead transferring all of the energy into the host rock, brecciating country rock and recycling water and lithic and juvenile material within the diatreme (Graettinger et al., 2014; Valentine et al., 2014; Sonder et al., 2015).

In areas where the water table is deeper than ~200 m, the implication is that explosions may occur but few are large enough to eject material and begin to develop a crater. However, maars are observed in areas where the water table is deeper than 200 m. This necessitates a mechanism to make water available for MFCI at depths above the water table. One way is for subsurface jets of explosion debris to transport groundwater upward (White and McClintock, 2001; McClintock and White, 2006; Ross and White, 2006). In this paper, we explore another potentially important mechanism, which involves redistribution of water in the subsurface due to heat of magma intrusion. We demonstrate this using parameters relevant to two maars in the San Francisco Volcanic Field (Arizona, USA) that formed despite the deep (~350 m) water table at their locations.

2. Approach and Methods

2.1. Numerical simulation of thermohydrologic processes

We used the TOUGH2 numerical simulator (Pruess et al., 2011) to explore thermally-induced redistribution of groundwater in maar-diatreme systems. Our simulations are aimed at testing possible pre-eruptive and syneruptive thermohydrologic processes at maar-diatreme volcanoes. TOUGH2 does not model the MFCI itself, but it does simulate how water (as vapor and liquid) can ascend, driven by magmatic heat and a heat pipe mechanism, to set up the conditions for shallow explosive interaction. The heat-pipe process has been extensively studied for its ability to enhance heat transfer in geothermal systems (e.g., Schubert and Straus, 1979; Pruess, 1985; Udell, 1985; Hurst et al., 1991).

2.2. TOUGH2 Model Setup

TOUGH2 is a numerical simulator for non-isothermal, multiphase fluid flow in fractured and porous media (Pruess et al., 2011). The simulator solves mass and energy balance equations for fluid and heat flow in space- and time-discretized systems, with the assumption of local thermodynamic equilibrium of all phases. Capabilities of the software extend to numerous geological and hydrogeological applications through a variety of equation-of-state (EOS) modules, each of which is representative of specific fluid mixtures, or components, for which the modules provide the necessary thermophysical properties for mass and energy balance equations. The module used for this work is EOS3, which models non-isothermal water and air transport including boiling and condensation of water. We invoked TOUGH2/EOS3 from iTOUGH2 (Finsterle, 2007) which provides enhanced control features for TOUGH2 simulation runs.

Although TOUGH2/EOS3 does not include the capability to represent supercritical water ($P_{crit} > 22$ MPa, $T_{crit} > 374$ ºC), it was used to investigate maar-related hydrologic processes with

118   the understanding that modeled temperatures are lower than would be realistically expected in

119   volcanic eruptions, but that the processes of vaporization, upward vapor flow, condensation, and

120   downward liquid water flow would be qualitatively analogous at higher temperatures. A second

121   limitation to TOUGH2/EOS3 for modeling magmatic systems is that modeling full dry-out

122   (transition from single-phase liquid or two-phase (aqueous and gas) conditions to single-phase

123   gas) can cause convergence problems. Although we specify a non-zero liquid residual saturation

124   (S_{lr}, Table 1), this value only affects flow processes, and vaporization and boiling can reduce

125   aqueous phase saturation to values less than S_{lr}. Such dry-out conditions can lead to very small

126   time-step sizes associated with poor convergence due to grid blocks oscillating back and forth

127   within a time step between two-phase and single-phase conditions. When TOUGH2 converges

128   on the first iteration twice in a row but fails when the time-step is automatically doubled on the

129   next time step, the TOUGH2 simulation automatically stops, resulting in arbitrary end times for

130   some simulations. This explains the different end times of the various simulations summarized in

131   the *Results* section.

132   The TOUGH2 computational mesh representing the discretized physical system

133   comprises grid blocks that are each assigned primary thermodynamic properties: pressure (P),

134   temperature (T), and gas saturation (S_g) for EOS3, and material properties including

135   permeability, porosity, and specific heat capacity. For the simulations carried out in this study,

136   all mesh files are two-dimensional and 1 m thick in the *y*-direction (i.e., 2D Cartesian), which is

137   appropriate for the case in which magma is intruded as a long dike trending perpendicular to the

138   grid. The standard mesh design is a "zoomed in" view from the upper portion of the aquifer to

139   the ground surface (Fig. 2). It is 300 m wide and 425 m deep, extending ~80 m below an

140   approximately 345-m-deep water table. A second mesh extending 1200 m wide and 710 m deep

141   was also used to test the two base-case scenarios on a larger scale. We use a uniform mesh with

142   fine resolution (grid-block size 20 m × 10 m) for all of the grid except for the upper 75 m of the

143   standard models (Kaibab Formation, Table 2) and the lower 285 m (Supai Group) in the large

144   models, in which grid blocks are 20 m × 15 m. The grid resolution was chosen to resolve the

145   main heat and mass flow processes to demonstrate the mechanism of water re-distribution by

146   heat pipe.
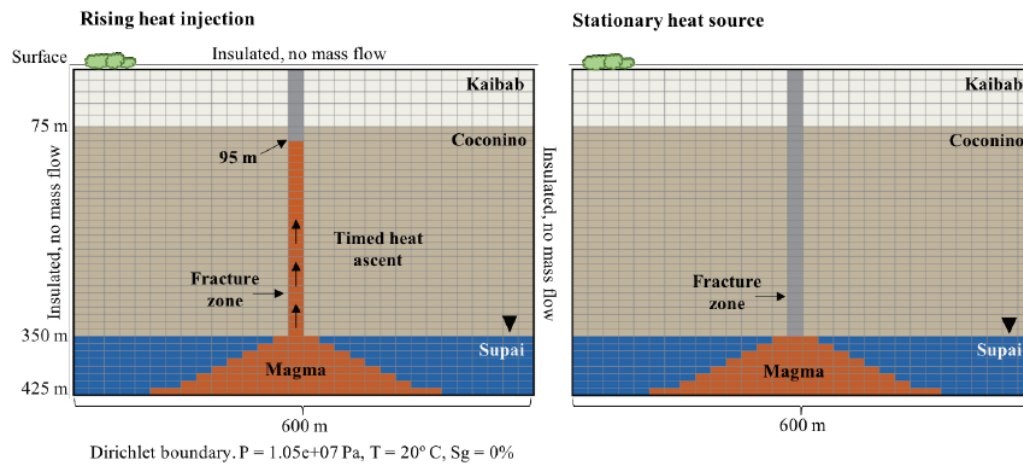
Figure 2: Schematic diagrams showing the setups for models with rising heat injection (left) and those with a stationary heat source (right). The 1-m-thick magma dike at the base is approximately 360-m-wide, tapering up to 60-m-wide at the water table, and 20-m-wide within the fracture (up to 95 m depth) in the rising heat simulations. All orange blocks receive heat injection (5.50×10^5 J/s). In the rising heat simulations, heat is injected into rows of grid blocks, moving upward, at a rate corresponding to a magma ascent rate of 0.5 m³/s. Boundary conditions labeled in the left diagram are the same in all models.

147

148   Initial model runs were performed to establish static steady-state gravity-capillary

149   equilibrium water saturation profiles in the unsaturated (two-phase) subsurface prior to any heat

150   input, and the final steady-state conditions from these simulations were then used as the starting

151   conditions for simulations with heat injection representing magma intrusion. A 20-m-wide

152   "fracture zone," or a high-permeability, high-porosity feature, is located in the center of the

153   model, intended to represent the combined effects of numerous smaller fractures or a single high-

154   permeability zone of broken rock. For all heat injection simulations, the bottom boundary has

8

155 been assigned Dirichlet boundary conditions (i.e., constant P, T, and gas saturation), and the side

156 and top boundaries are closed to heat (insulated) and mass flow.

157   Numerous forward models were carried out to understand how specific rock and

158 thermodynamic parameters affect model outcomes. Ascending magma is modeled as heat

159 injection into specified grid blocks, described only by a heating rate (J/s) (Anderson, 2017)

160 (Appendix A). Total volume of liquid water moved above a depth of 205 m (the bottom depth of

161 the row of grid blocks with center points at 200 m) at the final timestep has been calculated for

162 some simulations, but we note these per-meter of dike volumes are strictly representative only of

163 the two-dimensional, 1-m-thick domain or a 3D equivalent (arbitrary length perpendicular to the

164 2D plane of the domain) and are not strictly valid where 3D effects are present, e.g., at the ends

165 of the dike (Anderson, 2017).

166   *2.3. System properties and scenarios*

167   The hydrologic and hydrostratigraphic properties of the modeled systems (Tables 2 and

168 3) are based on representative example cases, Colton Crater and Rattlesnake Crater. Our models

169 are not meant to specifically model all the conditions of these particular eruptions. Rather, we

170 use these extreme examples to help test whether heat pipes can provide a generally applicable

171 mode to move water through diatremes. The water table is estimated to be at depths of ~340-380

172 m beneath Colton Crater and ~315-350 m beneath Rattlesnake Crater, placing it in the lower

173 Coconino Sandstone or Upper Supai Group (Hoffman et al., 2006; Bills et al., 2000; ADWR).

174 The nearest well to Rattlesnake Crater (~1.5 km to the SW) places the water table at ~315 m

175 deep; the base-case groundwater depth of 345 m is therefore considered to be a lower limit for

176 conditions during its eruption. The water table was probably close to these levels at the time of

177 the eruptions in the Pleistocene (Moore and Wolfe, 1987); regional topography and elevation of

178   groundwater outflow into the Little Colorado River basin in the Pleistocene epoch are interpreted

179   to have been similar to present day (Holm, 2001), which allows the inference that groundwater

180   levels would have also been approximately the same. Permeability of the Coconino Sandstone

181   and Upper Supai Group were estimated based on modeled hydraulic conductivity values for

182   nearby wells (Hoffman et al., 2006). Initial parameters for gravity-capillary equilibrium runs are

183   given in Table 1, and all estimated country-rock properties are given in Table 3.

184   Simulations were created using one of two primary model setups: rising heat injection or

185   stationary heat injection (Fig. 2). Both models use the same calculated heating rate of 5.50×10^5

186   J/s for all heat injection. In the rising heat models, heat is injected row by row at timed intervals,

187   moving upward from the bottom boundary of the model toward the surface, imitating the ascent

188   of magma (Appendix A). The timing of heat injection was determined based on a magma ascent

189   rate correlating with a volumetric injection rate of 0.5 m^3/s, considered to be an approximate

190   minimum magma ascent rate for basaltic eruptions (Walker, 1973). Heat is injected up to 95 m

191   depth; once magma and water reach this depth, they are shallow enough for MFCI to eject

192   overlying material and the locus of explosion can then, theoretically, become the new surface.

193   The stalled heat injection models are set up with a dome-shaped heat source, or magma injection

194   that reaches from the base of the model to the water table. The region of heat injection for the

195   standard 425-m-deep model is 360 m wide at the bottom boundary and tapers to 60 m at the

196   water table (Fig. 2). The heat source does not move and the heating rate (5.50×10^5 J/s) is

197   continuous throughout the duration of each simulation. Note that the bottom of the simulation

198   domain is held at the initial temperature of 20 ºC, but overall simulation times are short (on the

199   order of days), so the high temperatures in the domain caused by heat injection are not altered

200   appreciably by heat loss from the bottom. In other words, over the time of magma intrusion and

201 heat-pipe processes that we simulated, and with insulated boundary conditions along the top and

202 sides and minimal effects arising from the bottom constant-temperature boundary condition, heat

203 loss out the bottom is minor.

204 Several input parameter variations were applied to the models to test the dependency of

205 model results on each parameter. These variations include: increased and decreased permeability

206 of rock units, increased permeability and porosity of the fracture zone/conduit, anisotropic

207 permeability of rock units, increased and decreased porosity, increased and decreased heat rate,

208 raised and lowered water table depth, and doubled fracture zone width (Anderson, 2017).

209 Selected test simulations are described in *Results*.

210 These two setups are not necessarily separate processes; a stationary-heating scenario

211 may occur prior to the first magma reaching the surface, or concurrent with magmatic eruption,

212 with sill and dike intrusion in the shallow subsurface. Le Corvec et al. (2018) modeled intrusions

213 into diatremes and show that the brecciation of the diatreme affects local stress states, inhibiting

214 magma ascent and driving its lateral diversion, which would enhance heat transfer in a heat pipe,

215 as in our slow-ascent simulations. While a narrow dike travels through a fracture or conduit to

216 the surface, the larger rising or stationary magma body at depth can continue transferring heat to

217 the surrounding country rock and groundwater. At any time in an eruption, dikes may branch

218 from the main conduit through pre-existing or newly opened fractures (e.g. Re et al., 2015;

219 Muirhead et al., 2016), where magma may then come into contact with transported groundwater

220 and induce MFCI.

221 To demonstrate the heat pipe process in a growing diatreme, we have created a series of

222 simplified simulations based on the formation of the Rattlesnake Crater diatreme to a depth of

223 710 m, using a growing region of high permeability to demarcate the diatreme shape (Fig. 3).

224   This is not representative of the entire diatreme beneath Rattlesnake Crater, as geophysical

225   analysis indicates that it extends to at least 800 m and possibly as deep as ~3 km (Marshall et al.,

226   2015). Case 3A begins at equilibrium, and heat (5.50×10^5 J/s) is injected in a dome-shaped

227   region from the base of the model to 345 m depth. The subsequent simulation (Case 3B) includes

228   a zone of high permeability in the center of the model up to the new saturation limit, representing

229   a region of brecciated country rock where first explosions might have occurred, and heat

230   injection reaches 95 m depth. In the last step of the series (Case 3C), a large, high-permeability

231   diatreme structure is added and the region of heat injection expands into the diatreme.
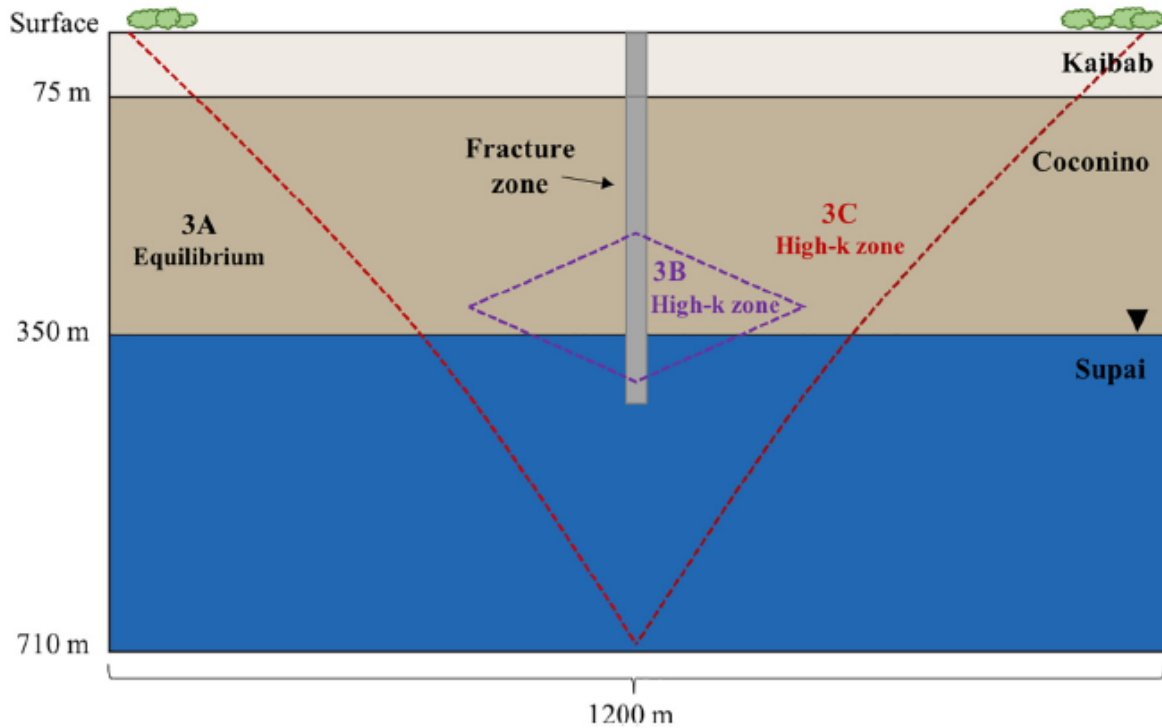
232

Fig. 3. Simplified schematic diagram showing changes to initial conditions in each step of the progressive diatreme growth simulation. Case 3A is started at equilibrium, Case 3B includes an added zone of high permeability (purple dotted line) to represent explosions occurring near the raised water table, and Case 3C includes a large-scale, high-permeability diatreme structure (red dotted line). (For interpretation of the references to color in this figure legend, the reader is referred to the web version of this article.)

233

3. Results

3.1. Rising Heat Injection

3.1.1. Case 1.1

Case 1.1 models timed heat injection into a mesh with a fracture zone extending from the ground surface to 425 m depth within the saturated upper Supai Group. Heat is injected up to 95 m depth over 660 seconds (eleven minutes). The simulation ran for ~3.1 days (Fig. 4) until convergence problems occurred related to dry-out (see Section 2.2). The highest pressure zones (up to 2.2×10^6 Pa) form around either side of the fracture-zone pathway within the liquid-saturated base of the model, while the fracture-zone pathway itself has a significantly lower pressure. Maximum temperatures reach ~500°C within the middle to upper fracture zone, but do

13

244   not exceed ~220˚C within the aquifer. The gas saturation plot shows how the water has moved as

245   a result of the injected heat. Around the heat injection in the saturated base and up into the

246   fracture zone, pore space contains 90-100% heated vapor by volume (i.e., grid block gas

247   saturation equals 90-100%) with the remainder liquid water (10-0%). In the center of the model,

248   the original water table is now raised, with grid blocks of 90-100% liquid saturation (10-0%

249   water vapor) now reaching upward to a depth of ~300 m. Grid blocks containing up to ~60%

250   liquid saturation are now present on either side of the fracture zone, nearly reaching the ground

251   surface. Vectors show strong upward vapor flow through the fracture zone, while smaller

252   magnitude vapor flows are seen on either side of the fracture pointing outward.
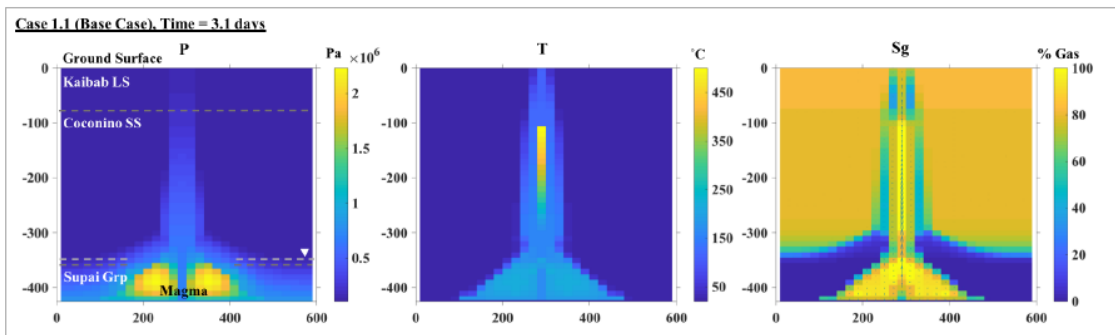

Figure 4: Pressure, temperature, and gas saturation at t ~ 3.1 days for a simulation with rising heat injection up to 95 m depth. A fracture zone extends from the ground surface to 425 m depth. Gas flow vectors, scaled relative to magnitude, overlain on S_g plot. Largest gas flow rate vector in fracture zones: $V_Z = 0.29$ kg/s, $V_X = 6.00 \times 10^{-6}$ kg/s. Dashed gray lines in the pressure diagram separate the geologic units, and the dashed white line shows the original water table.

253

254

255   3.1.2. Case 1A

256   In the large model of this scenario (Case 1A, supplementary files), heat is injected at the

257   same rate, corresponding to 0.5 m³/s of magma. A 600-m-wide zone in the bottom 45 m of the

258   model is heated at a constant rate throughout the run, and step-wise heat injection begins at 665

259   m depth at 30 seconds. The injection zone tapers to a width of 60 m at the water table. Results of

260   this simulation at 2.4 days show maximum pressure at the base of the aquifer, gradually

14

261 decreasing upward in the zone of heat injection. High temperatures and increased vapor

262 saturation develop in the upper aquifer, outside the cooler fracture zone. Just above, several

263 blocks of increased liquid saturation (>~70% aqueous phase, ~30% vapor) reach as high as 285

264 m depth. Zones of increased liquid saturation extend up to 40 m laterally away from the fracture

265 zone within the unsaturated Coconino Sandstone, and near the Kaibab boundary, liquid

266 saturation reaches ~50%.

267

268   3.1.3. <u>Case 1B</u>

269   Case 1B tests increased country-rock permeability relative to the base case. The

270 Coconino Sandstone permeability is increased to 8.97×10^{-11} m^2, and the same permeability and

271 density are given to the upper Supai Group. Boundary blocks have also been given the same

272 density as the Coconino Sandstone and aquifer of 2,450 kg/m^3, and a porosity of 15%. Results of

273 this simulation at 2.1 days (when dry-out caused poor convergence) are shown in Fig. 5

274 alongside those for the base case (Case 1.1) at the same time in the experiment. The high-

275 permeability model shows a wider area of impact around the heat injection, but total pressure and

276 temperature are generally lower. Vapor and associated condensation reach outward 40 m

277 laterally from the fracture zone up to nearly 100 m depth.
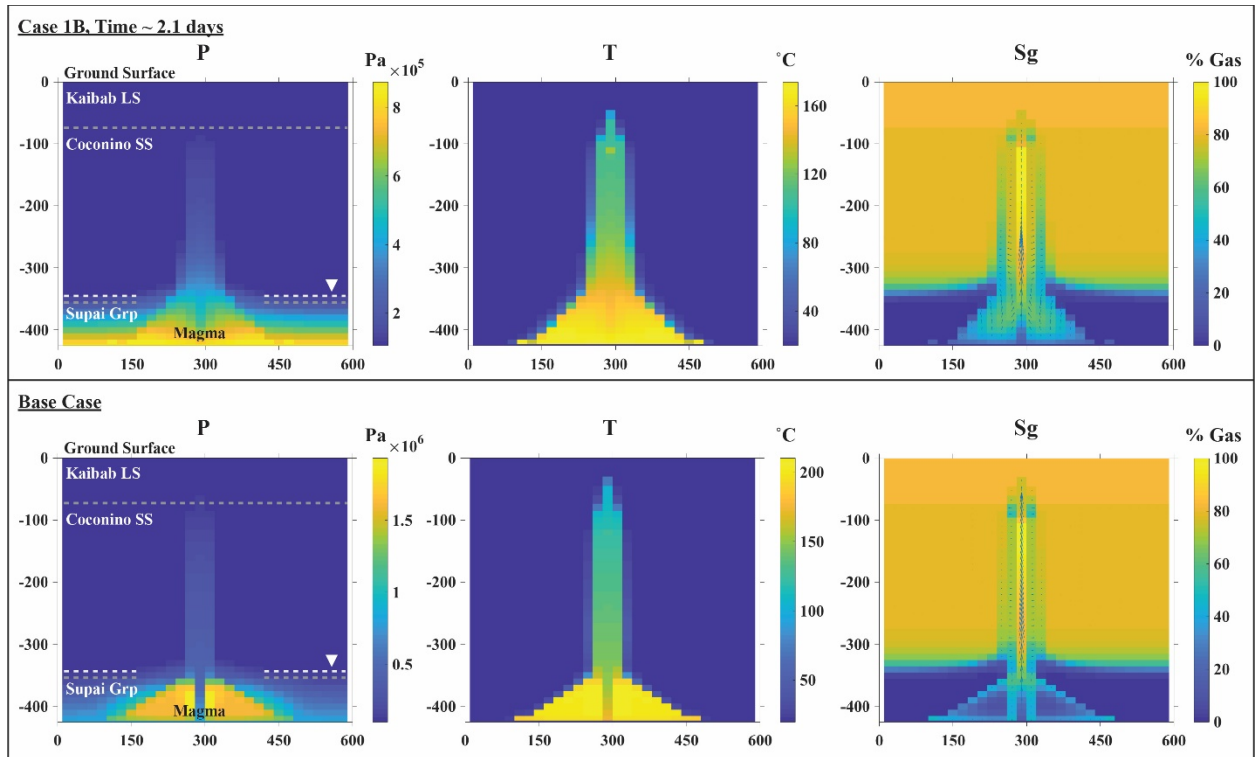
Figure 5: Pressure, temperature, and gas saturation at ~2.1 days for rising heat injection simulations with increased country rock permeability (Case 1B, top) and base-case conditions (Case 1.1, bottom). Color scale ranges spanning the max/min P and T are not uniform between models, as this results in significant loss of detail for some simulations. Gas flow vectors overlain on S_g plot are scaled relative to magnitude. Largest gas flow rate vector in fracture zone: $V_z = 0.34$ kg/s, $V_x = -7.53 \times 10^{-6}$ kg/s (Case 1B). Dashed gray lines in the pressure diagram separate geologic units, and the dashed white line shows the original water table.

3.2. Stationary Heat Source

3.2.1. Case 2.1

Case 2.1 models stationary heat injection into a system with a fracture zone extending

from the ground surface to 425 m depth (Fig. 6). The model runs for ~4.4 days and, as in the

rising-heat-injection models, the highest pressure zones are focused around either side of the

fracture zone within the aquifer. The center of the direct heat injection zone is primarily ~350-

450°C, with one block within the fracture zone at the depth of the original water table reaching

~500°C. Gas saturations show a zone of heated vapor in the center of the injection, with liquid

16

295   water, some of which is barely heated above equilibrium temperature, being driven upward. On

296   either side of the fracture zone at a depth of 290 m, grid blocks previously at residual saturation

297   reach a liquid saturation of ~65%, and condensed water is present as far as 40 m away from the

298   fracture zone. Vectors show strong vapor flow toward the surface through the fracture zone. In

299   just over 4 days, an additional ~270 m^3 of liquid water is emplaced above a depth of 205 m in

300   this two-dimensional scenario.
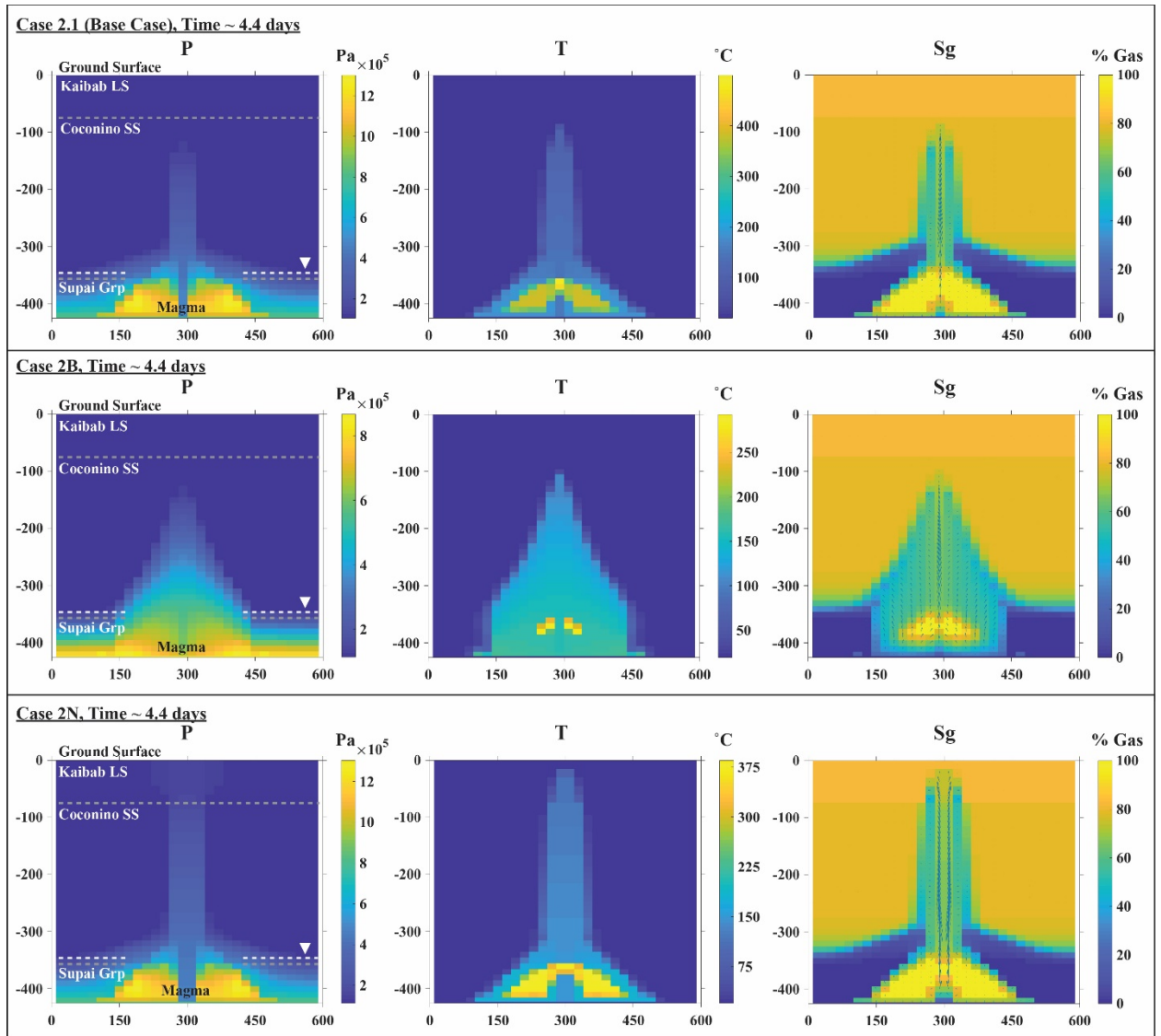
Figure 6: Pressure, temperature, and gas saturation at ~4.4 days for stationary heat injection simulations under base-case conditions (Case 2.1), with increased country-rock permeability (Case 2B), and with doubled fracture zone width (Case 2N). Color scale ranges for *P* and *T* are not uniform between models, as this results in significant loss of detail for some simulations. Gas flow vectors overlain on *Sg* plots are scaled relative to magnitude. Largest gas flow rate vectors in fracture zone: $V_Z = 0.15$ kg/s, $V_X = 4.45 \times 10^{-6}$ kg/s (Case 2.1). Dashed gray lines in the pressure diagram separate geologic units, and the dashed white line shows the original water table.

3.2.2. Case 2A

The large model of stationary heat injection at standard conditions (Case 2A, supplementary file) is set up with constant heat injection in a dome-like shape. The base of the

18

314   injection is 600 m wide at 710 m depth, tapering upward to 200 m at 530 m depth. The model

315   runs to ~8.1 days before TOUGH2 stops due to dry-out. Highest pressure is focused within the

316   central and lower heated region, surrounded by a gradual pressure gradient up to the top of the

317   saturated zone. The water table has shifted upward from 345 m depth; grid blocks with as much

318   as 50% liquid water reach 275 m depth, decreasing to <30% liquid by 245 m. The heat injection

319   region itself is entirely vapor at ~8.1 days, surrounded by a thin rim of two-phase liquid and

320   vapor.

321

322   ### 3.2.3. Case 2B

323   We tested the sensitivity of simulation results to the assigned permeability values for the

324   geologic units. As in the rising heat injection models, permeability was increased for the

325   Coconino Sandstone and saturated upper Supai Group to 8.97×10^{-11} m^2 (Case 2B). Conditions

326   at the end of the simulation at 4.4 days are shown in Fig. 6 compared to the base case (Case 2.1)

327   at the same time. A large tear-drop-shaped zone of vapor and associated condensed water is

328   present within the sandstone, affecting grid blocks as high as ~95 m below the surface. Just

329   above the water table, the zone extends ~420-460 m wide. Most of the affected grid blocks

330   contain less than ~75% vapor saturation, or greater than 25% liquid water saturation, and most of

331   the model remains below 200˚C.

332

333   ### 3.2.4. Cases 2C & 2D

334   Lower permeabilities were tested in Cases 2C and 2D. Permeabilities of the Coconino

335   Sandstone and upper Supai Group are lowest in Case 2C. The simulation runs to just under 4

336   days (Fig. 7). Heat and fluid flow are largely restricted to the fracture zone, but vapor does form

337   within the aquifer, and a small area of rising saturation is seen around the fracture zone just

338   above the water table. Water begins condensing around the fracture zone, but blocks do not

339   exceed 50% liquid saturation above ~100 m depth. The highest pressures are more than an order

340   of magnitude greater than under base-case conditions. In Case 2D, permeabilities for Coconino

341   Sandstone and the upper Supai Group are an average of the base-case and 2C permeabilities.

342   Results of this simulation at ~4 days vary little from the base case (supplementary figures).
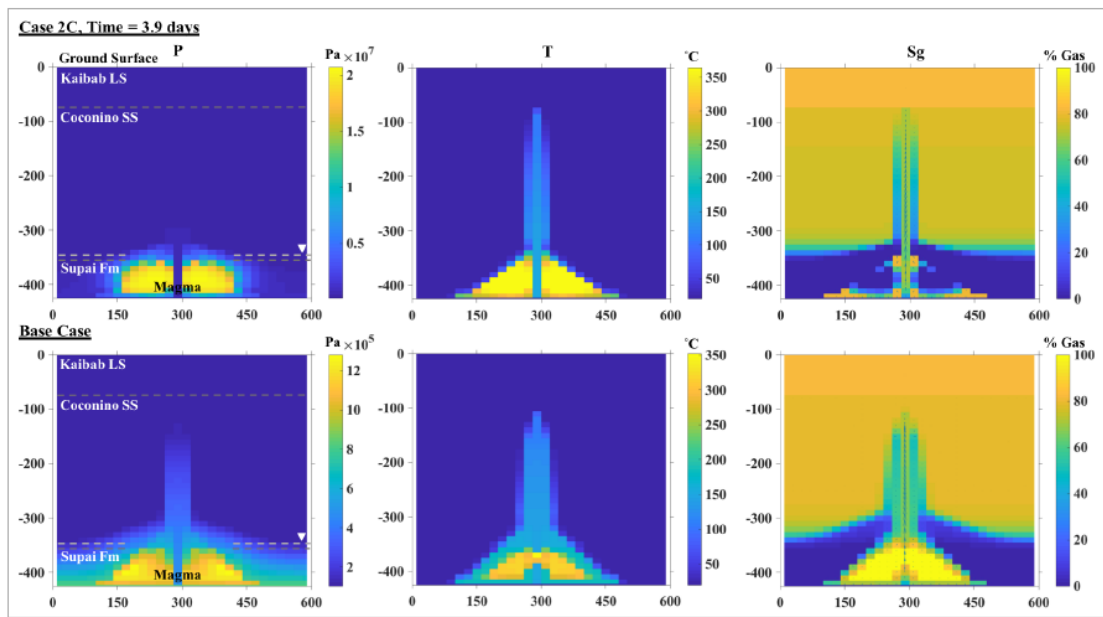
Figure 7: Pressure, temperature, and gas saturation at ~3.9 days for stationary heat injection simulations with low (Case 2C) and base-case permeabilites. Gas flow vectors overlain on S_g plots are scaled relative to magnitude. Largest gas flow rate vector in fracture zone: $V_Z = 0.25$ kg/s, $V_X = 0$ kg/s (Case 2C). Dashed gray lines in the pressure diagram separate the geologic units, and the dashed white line shows the original water table.

343

344

345   3.2.5. <u>Case 2N</u>

346   Fracture-zone width is doubled to 40 m in Case 2N, and parameters for this model at ~4.4

347 days are shown in Fig. 6. Increased fracture zone size has little effect on general pressure and

348 temperature conditions, but T_{max} is dropped to below 400˚C. In ~4.4 days, a column of two-phase

349 fluid 120 m wide (including the fracture zone) reaches the Kaibab-Coconino boundary at 75 m,

350 and a narrowing column continues into the Kaibab limestone up to ~15 m depth. A total of 1,560

351 m³ of liquid water is brought up above 205 m depth (in the two-dimensional space). Allowing

352 the simulation to continue to ~5.3 days shows a total of 1,780 m³ of liquid water brought to this

353 depth, or an additional 220 m³ in less than a day.

354   ***3.3. Diatreme Formation***

355   A simplified demonstration of the heat pipe process in a growing diatreme is modeled in

356 Cases 3A-3C (Fig. 8). In Case 3A, heat is injected from the base of the model up to 345 m depth.

357 After ~4.4 days, a zone of grid blocks containing >70% liquid saturated reaches ~235 m depth. A

358 zone of high permeability is added in the new saturated region and heat is injected up to 95 m

359 depth in Case 3B. After ~11 minutes, gas vectors show strong flow into and outward from this

360 region. A large, high-permeability diatreme structure is opened in the last step (Case 3C), and

361 heat injection expands into this region. After just over 20 minutes in the final simulation, vapor

362 and liquid water have begun to spread out to the walls of the diatreme and to the surface. It is

363 important to emphasize the change in time scale from days to minutes once the brecciation of the

364 diatreme occurs.
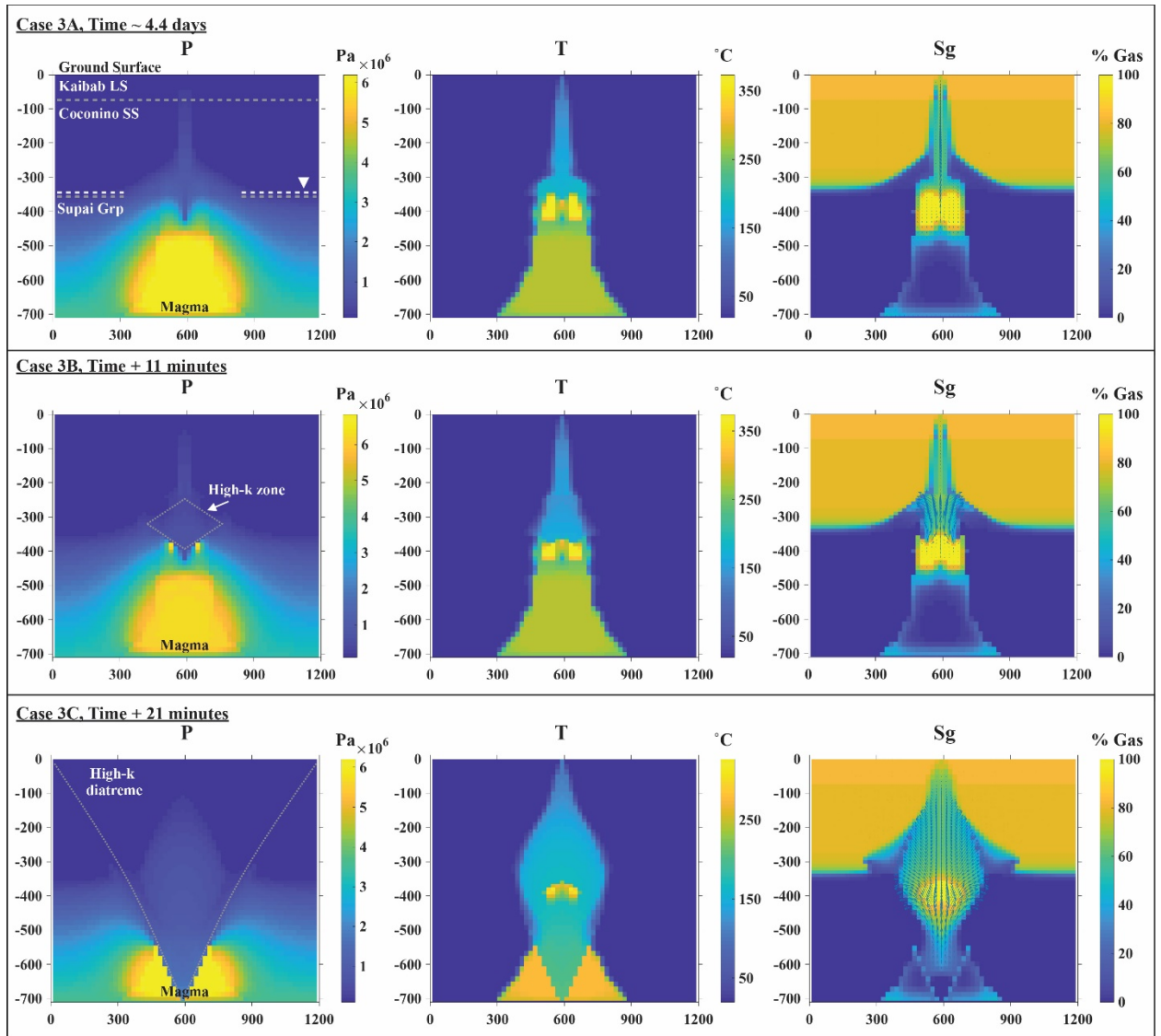
Figure 8: Pressure, temperature, and gas saturation for the simplified progressive diatreme growth simulation. Case 3A (top) shows magma injection up to 345 m depth after ~4.4 days. Case 3B (middle) is a continuation of Case 3A, with an additional zone of high permeability (as shown in 8A) and heat injection up to 95 m depth, and Case 3C (bottom) is a continuation of Case 3B with a high-permeability diatreme structure (as shown in 8A) and an expanded zone of heat injection into the high-permeability area. Color scale ranges for *P* and *T* are not uniform between models, as this results in significant loss of detail for some simulations.

4. Discussion

All of the models show that liquid water, driven upward as heated vapor, can condense around the outside of a permeable fracture zone, magma conduit, or diatreme prior to and during

22

377   an eruption under a range of conditions. The rising-heat-injection scenarios show how water and

378   vapor may move around a super-heated fracture zone or conduit during the earliest stages of an

379   eruption, while stationary-heat-injection models demonstrate thermohydrologic processes that

380   may occur near the water table with the presence of a hot magmatic body in an aquifer. Base-

381   case models show a zone of condensation reaching 40-60 m outside the conduit after only ~3-4

382   days, and a halo of increased saturation reaching ~50 m above the equilibrium water table. As

383   eruptive episodes often last days to weeks, or even years, injecting dikes and sills below the

384   volcano, it is likely that these processes would continue at a similar rate to transport even greater

385   quantities of water upward, where it can then condense and be temporarily held by capillary

386   forces or within fractures and voids. When magma then rises quickly toward the surface and

387   erupts, a potentially large volume of liquid water may be available at shallow enough depth to

388   produce sustained, ejecta-producing explosions. Shallow intrusions, such as sills and dikes, are

389   common under maars (e.g. Re et al., 2015; Muirhead et al., 2016). Our modeled setup, with a

390   shallow, dome-shaped heat source, provides an indication of how these shallow dike/sill

391   complexes may affect water movement.

392   Models show water redistribution can occur under a range of subsurface conditions, with

393   efficiency largely dependent on permeability, fracturing, and time (Anderson, 2017). The lateral

394   and vertical extent of the ascending vapor halo increases with permeability and porosity, while

395   the amount of time it takes to be driven upward is inversely related to these parameters. The

396   calculated Coconino Sandstone permeability is high compared to other published sandstone

397   permeabilities (Bear, 1988), largely because of its significant fracturing in the study area. The

398   tested low-end permeability values (Cases 1D and 2D) are most comparable to moderately

399   fractured or non-fractured sandstone, while the tested higher-permeability values (Cases 1B and

400 2B) are most similar to a very fine, unconsolidated sand (Bear, 1988), similar to the lower

401 Bidahochi Formation, the country rock for the maars of the Hopi Buttes volcanic field (e.g.,

402 Lefebvre et al., 2013). In lower-permeability rocks, a fracture zone or otherwise high-

403 permeability feature appears necessary to allow vapor and water to be driven toward the surface.

404 Simulations doubling the width of the fracture zone/conduit from 20 to 40 m showed more than

405 three times the amount of water brought above 205 m than in the base case, with vapor reaching

406 as high as 15 m from the surface (Fig. 6). In natural conditions with three dimensions, we can

407 expect similar increases in water transport as dike length increases. Regardless of initial country-

408 rock permeability, the first explosions in a maar eruption will substantially change permeability

409 and porosity conditions as surrounding country rock is brecciated and overall permeability

410 increases; these processes should be modeled in future studies.

411   The heat rate (J/s) is dependent on estimated or averaged variables, and therefore includes

412 significant uncertainty. It is reasonable for these simplified models, but considering that magma

413 injection is only described by this rate, and heat rate should vary during eruption and between

414 different rock types, this parameter is open to variation. Increasing and decreasing heat rate by

415 nearly half an order of magnitude produces similar results to the base case, but at much different

416 rates (Anderson, 2017). A lower heat rate may take ~2 weeks or more to produce a result similar

417 to what is seen in ~3-4 days in the base case, and increasing it by the same magnitude produces

418 similar or nearly identical results in ~40% less time (1.8 – 2.3 days). The models with a higher

419 heat rate are probably most similar to actual direct heat from magma at very shallow depth

420 immediately prior to eruption, while lower heat rates are probably most comparable to a magma

421 body intruded well below the water table.

422

4.1. Colton & Rattlesnake Crater Eruptions

424   The eruption of Colton Crater was dominated by Strombolian activity, producing a large

425 scoria cone (Cummings, 1972), until late in the eruption when magma interacted with liquid

426 water and the resulting large explosions ejected much of the core of the existing scoria cone (Van

427 Kooten and Buseck, 1978), redepositing it on the outer flanks of the cone as a ~20-30-m-thick

428 massive bed of scoria and broken lava clasts. After a few small surge-producing events, the

429 eruption then quickly dried out again, producing a small scoria/spatter cone inside the crater

430 before the eruption ceased.

431   The conditions that caused or allowed water to come into contact with the magma remain

432 uncertain, but the limited phreatomagmatic tephra sequence at Colton Crater suggests this period

433 of activity did not last long. Evidence of northward vent migration is preserved in the scoria-cone

434 deposits (Leudemann et al., 2013), so perhaps the vent intersected a water-filled fracture in the

435 Kaibab or Coconino Formations. The phreatomagmatism was also near the end of the eruption,

436 so it is possible that magma flux had begun to wane and allowed water in the country rock to

437 flow toward the vent rather than driving it away as vapor. In either case, the modeled

438 thermohydrologic processes provide one possible mechanism for supplying shallow liquid water

439 for the Colton Crater eruption (Fig. 9). Abundant fractures present throughout the Coconino and

440 Kaibab Formations could have allowed for transport of even greater quantities of water than

441 observed in the idealized models, especially over the course of weeks or months that Colton

442 Crater erupted prior to magma-water interaction. Other factors that contributed to changes in

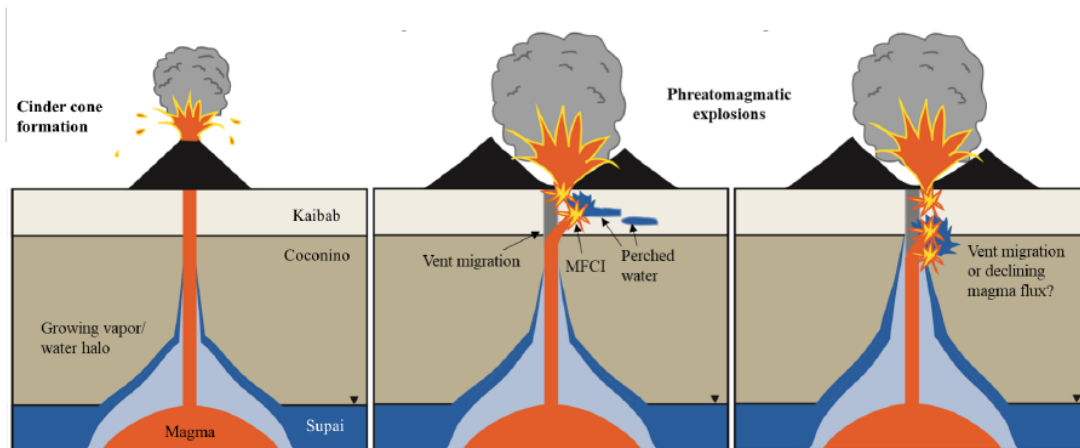443 behavior are beyond the scope of this research.

Figure 9: Schematic diagram showing possible scenarios for the eruptions of Colton and Rattlesnake Crater. Both eruptions started with Strombolian activity, building a scoria cone. Magmatic heat could have driven vapor (light blue) upward to the shallow subsurface, where it could condense to liquid (dark blue). Vent migration, branching dikes, or declining or stalled magma flux could have resulted in magma meeting condensed water and inducing MFCI.

444

445   The Rattlesnake Crater eruption appears to have started with a brief period of

446   Strombolian activity, but little of the initial scoria cone remains, buried beneath phreatomagmatic

447   tuff (Schwoerer, 2014). Most of the eruption consisted of repeated phreatomagmatic explosions

448   over a period possibly lasting weeks to months, followed by another stage that built a small

449   scoria cone on the southeastern crater rim. The crater and scoria cone vents trend northwest,

450   consistent with regional faulting. With an initially dry eruption, Rattlesnake Crater's behavior

451   was probably most similar to the rising heat injection model, with magma rising quickly to the

452   surface and driving away water as steam, rather than interacting with it. The presence of magma

453   below the water table during and potentially before the onset of eruption would have vaporized

454   aquifer water, which moved toward the surface to condense at shallow depths around the

455   conduit, similar to the stationary heat model. When the eruption transitioned to phreatomagmatic

456   activity after a short time, a significant quantity of water would have been available in the

457   shallow subsurface for sustained, efficient MFCI (Fig. 9).

458   As first explosions occurred in these eruptions, country rock would have been brecciated

459   and mixed with juvenile material and condensed water, creating a rapidly evolving setting for

26

460   these vapor transport processes. Feeder dikes probably deviated many times within the

461   permeable diatreme fill, resulting in continued heating, water redistribution, and explosions from

462   many locations within the diatreme, as demonstrated in Case 3 (Fig. 8). The important feature of

463   this model is that, once a diatreme starts to form, it appears to provide a very efficient pathway

464   for heat pipes to transport water vapor and liquid. Thus, once a maar-diatreme forms, it may

465   help provide its own water to itself for MFCI activity.

466

467   *4.2. Continuous Water Supply*

468   The observed results of these modeled scenarios may help to explain different behaviors

469   that have been recorded in eruptions around the world. As described, the process of vaporization

470   and related upward transport and condensation could provide shallow water to phreatomagmatic

471   eruptions in locations similar to the SFVF, where the water table is deep and well below the

472   estimated ideal depth for tephra-producing explosions.

473   A possibly more significant implication of this work is that these processes are probably

474   also important in locations where the water table is not deep; in these situations, they help

475   perpetuate eruptions that would otherwise "dry out" quickly. The cone of depression scenario of

476   Lorenz (1986) may occur in locations where very low country-rock permeability prevents

477   groundwater recharge to the diatreme on the time scale of the eruption. However, the TOUGH2

478   models show that movement of vapor and liquid water within and around the permeable, dike-

479   rich diatreme (Le Corvec et al., 2018), driven by the heat itself, could provide water to potential

480   explosion loci throughout the diatreme (Fig. 10). With dikes forming a complex network within a

481   diatreme breccia with broadly distributed water, the consequent explosions can happen anywhere

482   within a diatreme, both deep and shallow, where magma is intruded. Some dikes will be

27

483   emplaced non-explosively, as described by Lefebvre et al. (2013), but others will cause

484   explosions through rapid ascent and interaction with this intra-diatreme water.
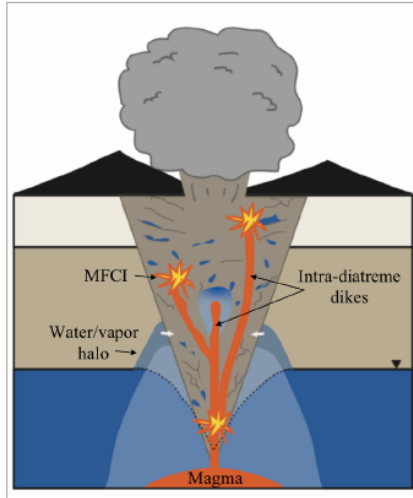

Figure 10: The modeled processes may help drive shallow explosions throughout an eruption as diatreme fill (taupe) is heterogeneously saturated, or in settings where the water table itself may be depleted during an eruption (dotted line). Upward vapor transport may provide condensed liquid water to many locations throughout the diatreme and surrounding area, which can then interact with intra-diatreme dikes and produce explosions.

485

486   Upward movement of water within the diatreme has often been attributed to debris jets

487   and recycling of material with explosions, processes that certainly occur and provide some

488   shallow water for explosions. The processes modeled here are capable of liquid and vapor

489   transport during and prior to eruption at a larger scale than would be expected by these

490   processes, especially in situations where magma may reside at a shallow depth for days to weeks.

491   The models may also explain phenomena like what occurred in 1759 in the first few

492   weeks of the El Jorullo eruption in central Mexico, where hot mud poured out of springs and

493   hillsides as phreatic and phreatomagmatic explosions occurred at the vent (Gadow, 1930).

494   Similar expulsions of hot water occurred at Mont Pelée (Martinique) in 1902, and meter-scale

495   increases in water levels in wells occurred at Mayon (Philippines) in 1993 and Usu (Japan) in

496   2000 (Pallister and McNutt, 2015). Calahorrano-Di Patre et al. (2019) describe hydrothermal

497   fluid migration into a shallow aquifer due to magma intrusion at Cotopaxi in 2015. In models

498 with highly permeable subsurface material, the wide halo of vapor and water reaches shallow

499 depths in just a few days even with a deep water table. If groundwater depth is ~100-200 m deep,

500 this time could be reduced to less than a day—especially if water and vapor follow fractures and

501 springs. The occurrence of this type of phenomena could also provide clues about the size of the

502 shallow magma source in an eruption.

503

504 **5. Conclusions**

505   Pre-eruptive and early eruption simulations created using TOUGH2/EOS3 provide

506 possible explanations for the occurrence of sustained phreatomagmatic activity in areas with

507 unusually deep groundwater, as well as a possible mechanism for providing a continuous,

508 shallow liquid water supply to an eruption. Simulations show that magmatic heat prior to and

509 during an eruption can drive a significant quantity of water toward the ground surface as heated

510 vapor, which then condenses to liquid water upon reaching cooler temperatures at shallower

511 depths. Once explosions brecciate and mix diatreme fill, increased permeability allows these

512 processes to increase in rate and efficiency. With liquid water placed in the shallow subsurface or

513 throughout a diatreme, rapidly ascending magma at the onset of eruption or interaction with

514 branching intra-diatreme dikes can initiate explosive MFCI to drive and sustain a

515 phreatomagmatic eruption. Rapid, large-scale vapor transport and condensation can also explain

516 the voluminous outpouring of hot, muddy water that occurs with eruptions at some volcanoes.

517 Future investigation of these processes could be bolstered by experiments, geophysical analysis

518 of subsurface fracturing and structure, and/or detailed larger-scale modeling including

519 geomechanical processes and potentially eruption processes.

520

REFERENCES

1. Ai, H., Ahrens, T.J., 2004. Dynamic tensile strength of terrestrial rocks and application to impact cratering. Meteoritics and Planetary Science 39 (2), 233-246.

2. Anderson, E.S., 2017. An investigation of the role of thermal conditions, hydrologic processes, and country-rock permeability in maar eruptions. MS thesis, Northern Arizona University, Flagstaff, Arizona, 148 p.

3. Arizona Department of Water Resources (ADWR), 1998-2017. GWSI-Groundwater Site Inventory. http://gisweb.azwater.gov/waterresourcedata/GWSI.aspx.

4. Auer, A., Martin, U., Németh, K., 2007. The Fekete-hegy (Balaton Highland Hungary) "soft-substrate" and "hard-substrate" maar volcanoes in an aligned volcanic complex— Implications for vent geometry, subsurface stratigraphy and the palaeoenvironmental setting. Journal of Volcanology and Geothermal Research 159, 225-245.

5. Bear, J., 1988. *Dynamics of Fluids in Porous Media*. New York: Dover, p. 136.

6. Bills, D.J., Truini, M., Flynn, M.E., Pierce, H.A., Catchings, R.D., Rymer, M.J., 2000. Hydrogeology of the regional aquifer near Flagstaff, Arizona, 1994-97. U.S. Geological Survey Water Resources Investigations Report 00-4122, 142 p.

7. Bralower, T., Bice, D., (n.d.). Heat capacity and energy storage, Earth 103: Earth in the Future. College of Earth and Mineral Science, The Pennsylvania State University. https://www.e-education.psu.edu/earth103/node/1005. July 5, 2019.

8. Calahorrano-Di Patrea, A., Williams-Jones, G., Battaglia, M., Mothes, P., Gaunt, E., Zureka, J., Ruiz, M., Witter, J., 2019 Hydrothermal fluid migration due to interaction with shallow magma: Insights from gravity changes before and after the 2015 eruption of Cotopaxi volcano, Ecuador. Journal of Volcanology and Geothermal Research, 387, 106667, https://doi.org/10.1016/j.jvolgeores.2019.106667.

9. Cummings, D., 1972. Mafic and ultramafic inclusions, Crater 160, San Francisco Volcanic Field, Arizona. Geological Survey Research 1972, USGS Professional Paper 800-B, B95-B104.

10. De Silva, S., Lindsay, J.M., 2015. Primary volcanic landforms in Sigurdsson, H., ed., *Encyclopedia of Volcanoes (2nd Edition)*. Academic Press, 273-297.

11. Eppelbaum, L.V., Kutasov, I., Pilchin, A.N., 2014. Thermal properties of rocks and density of fluids in *Applied Geothermics*, Lecture Notes in Earth System Sciences. Springer-Verlag Berlin Heidelberg, 99-149.

12. Finsterle, S., 2007. iTOUGH2 User's Guide. Lawrence Berkeley National Laboratory Report LBNL-40040, Updated Reprint, 130 p.

584
585   13. Gadow, H., 1930. *Jorullo: The history of the volcano of Jorullo and the reclamation of*
586   *the devastated district of animals and plants*. Cambridge University Press, 101 p.
587
588   14. Graettinger, A. H., Valentine, G. A., Sonder, I., Ross, P.-S., White, J. D. L., and
589   Taddeucci, J., 2014. Maar-diatreme geometry and deposits: Subsurface blast experiments
590   with variable explosion depth, Geochem. Geophys. Geosyst., 15, 740–764,
591   doi:10.1002/2013GC005198.
592
593   15. Hoffman, J.P., Bills, D.J., Phillips, J.V., Halford, K.J., 2006. Geologic, hydrologic, and
594   chemical data from the C aquifer near Leupp, Arizona. U.S. Geological Survey Scientific
595   Investigations Report 2005-5280, 42 p.
596
597   16. Holm, R.F., 2001. Cenozoic paleogeography of the central Mogollon Rim-southern
598   Colorado Platea region, Arizona, revealed by Tertiary gravel deposits, Oligocene to
599   Pleistocene lava flows, and incised streams. GSA Bulletin 113 (11), 1467-1485.
600
601   17. Hurst, A.W., Bibby, H.M., Scott, B.J., McGuinness, M.J., 1991. The heat source of
602   Ruapehu Crater Lake; deductions from the energy and mass balances. Journal of
603   Volcanology and Geothermal Research 46 (1-2), 1-20.
604
605   18. Le Corvec, N., Muirhead, J.D., White, J.D.L., 2018. Shallow magma diversions during
606   explosive diatreme-forming eruptions. Nature Communications 9:1459, DOI:
607   10.1038/s41467-018-03865-x
608
609   19. Lefebvre, N.S., White, J.D.L., Kjarsgaard, B.A., 2013. Unbedded diatreme deposits
610   reveal maar-diatreme-forming eruptive processes: Standing Rocks West, Hopi Buttes,
611   Navajo Nation, USA. Bulletin of Volcanology 75:739. DOI 10.1007/s00445-013-0739-9
612
613   20. Leudemann, L., Ort, M.H., Witter, M., 2013. Transition from strombolian to
614   phreatomagmatic activity due to scoria cone vent migration: Colton Crater, San Francisco
615   Volcanic Field, northern Arizona. Abstracts with Programs - Geological Society of
616   America 45 (7), p. 336.
617
618   21. Lorenz, V., 1986. On the growth of maars and diatremes and its relevance to the
619   formation of tuff rings. Bulletin of Volcanology 48, 265-274.
620
621   22. Lorenz, V., 2003. Maar-diatreme volcanoes, their formation, and their setting in hard-
622   rock or soft-rock environments. GeoLines 15, 72-83.
623
624   23. Manger, E., 1963. Porosity and bulk density of sedimentary rocks. Contributions to
625   Geochemistry, Geological Survey Bulletin 1144-E, 55 p.
626
627   24. Marshall, A., Connor, C., Kruse, S., Malservisi, R., Richardson, J., Courtland, L.,
628   Connor, L., Wilson, J., Karegar, M.A., 2015. Subsurface structure of a maar-diatreme and

associated tuff ring from a high-resolution geophysical survey, Rattlesnake Crater, Arizona. Journal of Volcanology and Geothermal Research 304, 253-264.

25. McClintock, M., White, J.D.L., 2006. Large phreatomagmatic vent complex at Coombs Hills, Antarctica: Wet, explosive initiation of flood basalt volcanism in the Ferrar-Karoo LIP. Bulletin of Volcanology 68, 215-239.

26. Moore, R.B., Wolfe, E.W., 1987. Geologic map of the east part of the San Francisco Volcanic Field, north-central Arizona, US Geological Survey Map MF-1960.

27. Morrissey, M., Zimanowski, B., Wohletz, K., Büttner, R., 2000. Phreatomagmatic fragmentation in Sigurdsson, H., ed., *Encyclopedia of Volcanoes (1st Edition).* Academic Press, 431-445.

28. Muirhead, J.D., Van Eaton. A.R., Re, G., White, J.D.L, Ort, M.H., 2016. Monogenetic volcanoes fed by interconnected dikes and sills in the Hopi Buttes volcanic field, Navajo Nation, USA. Bulletin of Volcanology 78:11, 1-16, DOI:10.1007/s00445-016-1005-8.

29. Ort, M.H., Carrasco-Núñez, G., 2009. Lateral vent migration during phreatomagmatic and magmatic eruptions at Tecuitlapa Maar, east-central Mexico. Journal of Volcanology and Geothermal Research 181, 67-77.

30. Pallister, J., McNutt, S.R., 2015. Chapter 66: Synthesis of volcano monitoring, in Sigurdsson, H., ed., *Encyclopedia of Volcanoes (2nd Edition).* Academic Press, 1151-1171.

31. Pruess, K., 1985. A quantitative model of vapor dominated geothermal reservoirs as heat pipes in fractured porous rock.

32. Pruess, K., Oldenburg, C., Moridis, G., 2011. TOUGH2 User's Guide, Version 2.1, LBNL-43134 (revised). Lawrence Berkeley National Laboratory, Berkeley, CA.

33. Re, G., White, J.D.L, Ort, M.H., 2015. Dikes, sills, and stress-regime evolution during emplacement of the Jagged Rocks Complex, Hopi Buttes Volcanic Field, Navajo Nation, USA. Journal of Volcanology and Geothermal Research 295, 65-79, DOI: 10.1016/j.jvolgeores.2015.01.009.

34. Ross, P.-S., White, J.D.L., 2006. Debris jets in continental phreatomagmatic volcanoes: A field study of their subterranean deposits in the Coombs Hills vent complex, Antarctica. Journal of Volcanology and Geothermal Research 149, 62-84.

35. Schubert, G., Straus, J.M., 1979. Steam-water counterflow in porous media. Journal of Geophysical Research: Solid Earth 84 (B4), 1621-1628.

36. Schwoerer, A.J., 2014. Eruptive history of Rattlesnake Crater, Arizona, San Francisco Volcanic Field REU. Abstracts with programs- Geological Society of America 46 (6), p.

675   550.

677 37. Sonder, I., Graettinger, A.H., and Valentine, G.A., 2015. Scaling multiblast craters:
678   General approach and application to volcanic craters. Journal of Geophysical Research:
679   Solid Earth, p. 6141-6158.

681 38. Udell, K.S., 1985. Heat transfer in porous media considering phase change and
682   capillarity—the heat pipe effect. International Journal of Heat and Mass Transfer 28, 485-
683   495.

685 39. Valentine, G.A., Graettinger, A.H., Sonder, I., 2014. Explosion depths for
686   phreatomagmatic eruptions. Geophysical Research Letters 41, 3045-3051.

688 40. Valentine, G.A., White, J.D.L., 2012. Revised conceptual model for maar-diatremes:
689   Subsurface processes, energetics, and eruptive products. Geology, online,
690   www.gsapubs.org, doi:10.1130/G33411.1.

692 41. Van Kooten, G.K., Buseck, P.R., 1978. Interpretation of olivine zoning: Study of a maar
693   from the San Francisco volcanic field, Arizona. Geological Society of America Bulletin
694   89, 744-754.

696 42. White, J.D.L., 1996. Impure coolants and interaction dynamics of phreatomagmatic
697   eruptions. Journal of Volcanology and Geothermal Research 74, 155-170.

699 43. White, J.D.L., McClintock, M.K., 2001. Immense vent complex marks flood-basalt
700   eruption in a wet, failed rift: Coombs Hills, Antarctica. Geology 29 (10), 935-938.

702 44. Zimanowski, B., Buttner, R., Dellino, P., White, J.D.L., Wohletz, K.H., 2015. Magma-
703   water interaction and phreatomagmatic fragmentation in Sigurdsson, H., ed.,
704   *Encyclopedia of Volcanoes* (2nd Edition). Academic Press, 473-484.

Appendix A

Model Software

The **TOUGH** ("**T**ransport **O**f **U**nsaturated **G**roundwater and **H**eat") suite of software codes are multi-dimensional numerical models for simulating the coupled transport of water, vapor, non-condensible gas, and heat in porous and fractured media. Developed at the Lawrence Berkeley National Laboratory (LBNL) in the early 1980s primarily for geothermal reservoir engineering, the suite of simulators is now widely used at universities, government organizations, and private industry for applications to nuclear waste disposal, environmental remediation problems, energy production from geothermal, oil and gas reservoirs as well as gas hydrate deposits, geological carbon sequestration, vadose zone hydrology, and other uses that involve coupled thermal, hydrological, geochemical, and mechanical processes in permeable media. The **TOUGH** suite of simulators is continually updated, with new equation-of-state (**EOS**) modules being developed, and refined process descriptions implemented into the **TOUGH** framework (see the overview of the **TOUGH** development history). Notably, EOS property modules for mixtures of water, NaCl, and CO_2 has been developed and is widely used for the analysis of geologic carbon sequestration processes. **TOUGH** and its application have been the subject of more than 500 peer-reviewed journal articles, conference proceedings, and project reports. **TOUGH** and its various modules are documented in a series of manuals. An example software validation report of TOUGH2 is provided in Pruess et al.

https://escholarship.org/content/qt0gq2w0r5/qt0gq2w0r5.pdf

Appendix A

Pruess, K., Simmons, A., Wu, Y.S. and Moridis, G., 1996. *TOUGH2 software qualification* (No. LBL-38383). Lawrence Berkeley Lab., CA (United States); Geological Survey, Denver, CO (United States).

More information about the TOUGH codes can be found here:

https://tough.lbl.gov/

For the simulations of water vapor transport and condensation related to maar volcanoes reported on in this paper, we used TOUGH2/EOS3, the equation of state module for water and air. In this module, water properties are calculated using the steam table equations from the International Formulation Committee, and air is approximated as an ideal gas (Pruess et al., 2011). The primary variables for EOS3 in two-phase conditions are pressure (P), temperature (T), and gas saturation (Sg). The number of mass and energy balance equations to be solved for each grid block of the computational mesh corresponds to the number of primary thermodynamic variables. With execution of the code, sets of coupled nonlinear equations for all grid blocks are solved simultaneously using Newton-Raphson iteration (Pruess et al., 2011).

Appendix A

Heat Flow Calculation

$q = -K(\Delta T/\Delta z)$
q = heat rate (J/s)
K = thermal conductivity........................... 2.1 W/m K
$\Delta T = T_{rock} - T_{magma}$.................................. 1000°C
$\Delta z = z_{rock} - z_{magma} = S_{TBL}$

$S_{TBL} = \sqrt{(\kappa\tau)}$
$\kappa = K/(\rho C_p)$
κ = thermal diffusivity (m²/s)
ρ = density of sandstone........................... 2500 kg/m³
C_p = heat capacity of wet sandstone...............920 J/kg K
τ = time scale...................................... 3600- 14400 s (1-4 hrs)**

1. $\kappa = K/(\rho C_p)$
   $= 2.1/(2500 \times 920)$
   $= 9.13 \times 10^{-7}$ m²/s

2. $S_{TBL} = \sqrt{(\kappa\tau)}$
   $= \sqrt{((9.13 \times 10^{-7})(3600))}$ *(2a)*
   $= 5.70 \times 10^{-2}$ m

   $= \sqrt{((9.13 \times 10^{-7})(14400))}$ *(2b)*
   $= 1.15 \times 10^{-1}$ m

3. $q = -K(\Delta T/\Delta z)$
   $= -2.1(-1000/(5.70 \times 10^{-2}))$ *(3a)*
   $= 3.66 \times 10^{4}$ J/s m²

   $= -2.1(-1000/(1.15 \times 10^{-1}))$ *(3b)*
   $= 1.83 \times 10^{4}$ J/s m²

4. Across whole 20 m² of interface (*i*):
   $q \times i = (3.66 \times 10^{4}) \times 20$ *(4a)*
   $= 7.33 \times 10^{5}$ J/s

   $= (1.83 \times 10^{4}) \times 20$ *(4b)*
   $= 3.66 \times 10^{5}$ J/s

   Average heat rate = **5.50 × 10⁵ J/s**

** Parameter was tested over a range of values; "final" or base-case heat rate is an average of these values.

Appendix A

Table A1: Schedules of heat injection with depth over time for the small models (left) and large models (right). After each injection start time, heat rate is continuous (5.50×10^5 J/s) for the remainder of the simulation.

Rapid Heat Injection Schedule- Small Model			
Injection depth (grid block top, m)	Injection width (m)	Vertical distance of magma travel (m)	Injection start time (s)
95	20	10	660
105	20	10	640
115	20	10	620
125	20	10	600
135	20	10	580
145	20	10	560
155	20	10	540
165	20	10	520
175	20	10	500
185	20	10	480
195	20	10	460
205	20	10	440
215	20	10	420
225	20	10	400
235	20	10	380
245	20	10	360
255	20	10	340
265	20	10	320
275	20	10	300
285	20	10	280
295	20	10	260
305	20	10	240
315	20	10	220
325	20	10	200
335	20	10	180
345	60	10	160
355	100	10	140
365	140	10	120
375	180	10	100
385	220	10	80
395	260	10	60
405	300	10	40
415	380	10	0
425	380	5	0

Rapid Heat Injection Schedule- Large Model			
Injection depth (grid block top, m)	Injection width (m)	Vertical distance of magma travel (m)	Injection start time (s)
95	20	10	1140
105	20	10	1120
115	20	10	1100
125	20	10	1080
135	20	10	1060
145	20	10	1040
155	20	10	1020
165	20	10	1000
175	20	10	980
185	20	10	960
195	20	10	940
205	20	10	920
215	20	10	900
225	20	10	880
235	20	10	860
245	20	10	840
255	20	10	820
265	20	10	800
275	20	10	780
285	20	10	760
295	20	10	740
305	20	10	720
315	20	10	700
325	20	10	680
335	20	10	660
345	60	10	640
355	100	10	620
365	140	10	600
375	180	10	580
385	220	10	560
395	260	10	540
405	300	10	520
415	340	10	500
425	380	10	480
440	380	15	450
455	420	15	420
470	420	15	390
485	420	15	360
500	460	15	330
515	460	15	300
530	460	15	270
545	500	15	240
560	500	15	210
575	540	15	180
590	540	15	150
605	580	15	120
620	580	15	90
635	580	15	60
650	620	15	30
665	620	15	0
680	620	15	0
695	620	15	0
710	620	7.5	0